optica

Diffractive oblique plane microscopy

Maximilian Hoffmann and Benjamin Judkewitz*

Charité Universitätsmedizin Berlin, Einstein Center for Neurosciences, NeuroCure Cluster of Excellence, Charitéplatz 1, 10117 Berlin, Germany
**Corresponding author: benjamin.judkewitz@charite.de*

Received 26 March 2019; revised 12 July 2019; accepted 12 July 2019 (Doc. ID 363426); published 3 September 2019

Imaging of neuronal activity with fluorescent indicators is an important technique in neuroscience. However, it remains challenging to record volumetric image data at fast frame rates and good resolution. One promising technique to achieve this goal is light sheet microscopy (LSM), but the right angle configuration of the excitation and imaging system limits its application. Oblique plane microscopy (OPM), a variant of LSM, circumvents this limitation by exciting oblique planes and detecting the image through the same microscope objective lens. So far, these techniques have relied on the use of high numerical aperture (NA) detection objective lenses, which limits their field of view. Here we present an OPM technique that allows for the use of low NA objective lenses by redirecting the light with the help of a diffraction grating. The microscope maintains a micrometer-scale lateral resolution over a large addressable imaging volume of 3.3 × 3.0 × 1.0 mm^3. We demonstrate its practicality by imaging the whole brain of larval and juvenile zebrafish.

https://doi.org/10.1364/OPTICA.6.001166

1. INTRODUCTION

Optical recording of neural activity has become an essential part of neuroscientific research. One of the most widely used techniques, two-photon microscopy [1], has an excellent resolution, is resilient to scattering tissue, and can record from a large field of view (FOV) [2,3], but its sequential detection scheme and the fluorescence lifetime limit the amount of neurons per unit of time it can record from. A number of techniques have thus been developed to increase volumetric imaging speed. Some techniques try to increase the excitation spot size of the two-photon scanning microscope [4,5], therefore reducing the number of points that have to be sampled. This enables faster acquisition rates from a given volume, but fundamentally remains subject to the limitations imposed by sequential detection. Other optical techniques achieve volumetric recordings by capturing a single snapshot on a camera sensor and thereby circumvent the limitations of sequential scanning schemes. This is achieved by multi-aperture imaging combined with computational reconstruction, as in light field microscopy [6–10] or by multiplexing and focusing different focal planes onto different sensor areas with the help of diffractive optics [11–13]. These camera-based techniques employ one-photon excitation, since the requirements on the total power of the light source as well as on the maximal permissive energy flux into the specimen can be more easily met. This sacrifices the confinement of the excitation volume of non-linear microscopy and leads to the loss of any optical sectioning capability, understood here as the "missing cone" in the 3D optical transfer function of the microscope [14]. One way to guarantee optical sectioning in linear microscopy is to break the collinearity of emission and excitation point spread functions (PSFs) as in light sheet microscopy or selective plane illumination microscopy (LSM/SPIM) techniques [15–17]. In LSM/SPIM, a light sheet perpendicular to the imaging objective excites the imaging plane. The excited fluorescence from an entire plane is then imaged onto a camera sensor by an imaging system situated at a right angle to the excitation beam. This requires the specimen to be accessible and optically transparent on both the imaging side as well as on the perpendicular excitation side, which is often not possible due to the cranium or other anatomical features of the organism of interest, such as the eyes in the case of fish.

Oblique plane microscopy (OPM) techniques circumvent these geometrical constraints by realizing lightsheet-type excitation and imaging through the same objective lens on oblique planes [18–26]. As a result, they require access to the sample from one side only (e.g., the top of the head for neuronal imaging). Exciting tilted planes decreases the angle between emission and excitation PSF [Fig. 1(a)], but still enables optical sectioning. For volumetric imaging, the oblique excitation sheet is scanned while the emitted light is descanned onto an oblique intermediate image plane. A high-speed OPM technique termed SCAPE achieves this with fast scanning mirrors and has been used to image neuronal calcium signals in mice and in larval Drosophila [21,27]. To avoid spherical aberrations associated with imaging of oblique planes, OPM methods employ a one-to-one magnification system [28]. The oblique intermediate image plane is then brought to lie perpendicular to the optical axis of a tertiary imaging system and can be captured in a conventional way by a camera. To maintain the FOV of the primary imaging system, the third objective lens has to have the same or lower NA, because optical design restrictions lead to an inverse relationship between objective NA and attainable FOV. This reimaging geometry inherently leads to losses, as parts of the light will not propagate

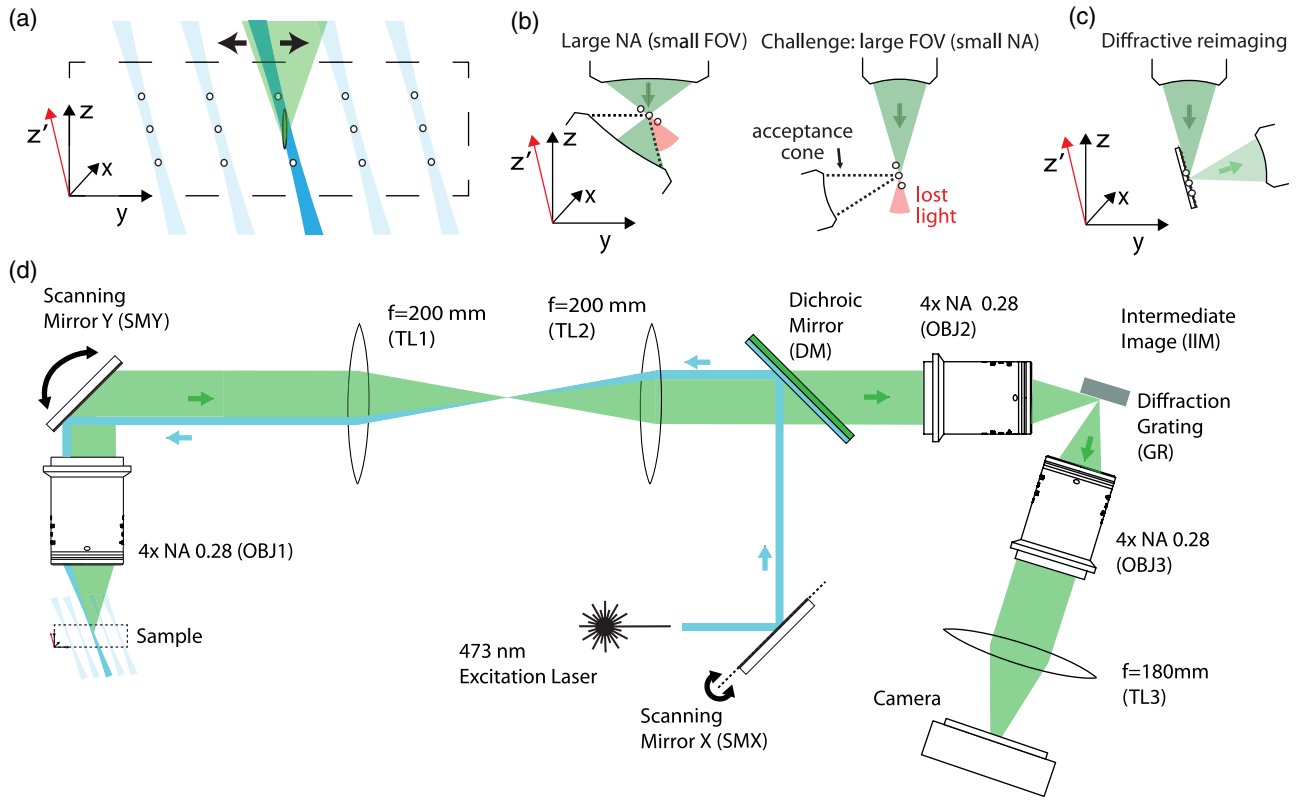

Fig. 1. Principle of operation. (a) Recording geometry of oblique plane microscopy: a swept Gaussian laser beam (dark blue) excites an oblique plane within the specimen (dashed box); the optical section is the result of the angle between the detection point spread function (PSF, green ellipsoid) and the excitation PSF (Gaussian beam). The emitted fluorescence light within the acceptance angle (green cone) is captured by the objective. Volumetric imaging is achieved by scanning the excitation light to parallel planes (light blue). The white circles represent sample points on the sheared volumetric grid and successive camera images. (b) Oblique reimaging for two different numerical apertures: an intermediate image plane (circles) is created and reimaged by two identical objectives. A part of the light cone emerging from the first objective (green) is not collected (red) because it does not propagate within the acceptance angle of the second objective. As the numerical aperture (NA) decreases, the light is completely lost. (c) Diffractive oblique reimaging: the inserted diffraction grating diffracts parts of the light into a direction almost perpendicular to the grating and allows reimaging at low NA. The angle of the grating matches the angles of the imaging planes in (b). (d) Setup: the laser focus at the galvanometric scanning mirror (SMX) is imaged onto a decentered spot at the backfocal aperture of the imaging objective OBJ1 by the $4f$ system consisting of the two tube lenses TL1 and TL2. This leads to an oblique incidence at the sample. Scanning the mirror SMX excites fluorescence in an oblique plane. The emitted fluorescence from the oblique plane is imaged onto a blazed diffraction grating (GR) at the intermediate image plane (IIM) with unit magnification by means of two identical imaging systems (OBJ1 TL1, OBJ2 TL2). The surface of the diffraction grating (GR) is imaged by a third imaging system (OBJ3, TL3) place perpendicular to the grating surface. The third imaging system collects the diffracted fluorescence at the IIM and images it onto the camera. A volume is imaged by scanning and descanning the imaging plane in the sample by scanning the galvanometric scanning mirror SMY.

inside the acceptance angle of the tertiary objective lens [Fig. 1(b)]. The loss becomes total at an NA ≤ 0.5 and prohibits the use of low-NA objectives, which are needed for large-FOV imaging. This has so far limited the FOV of OPM to $\leq 1 \times 1$ mm^2 [21,29].

Here, we overcome this limitation by employing a diffraction grating to allow oblique reimaging for low-NA objectives [30] and therefore enable OPM across a large FOV of 3.3×3.0 mm^2 [Fig. 1(c)].

2. METHOD

Our optical setup is schematically summarized in Fig. 1(d). Two identical imaging systems consisting of an imaging objective lens (XLFluor, 4 ×, 0.28 NA, corrected for a water layer of 0–5 mm, Olympus, used as OBJ1 and OBJ2) and a telecentric tube lens (TTL200MP, $f = 200$ mm, Thorlabs, used as TL1 and TL2) are placed back to back in order to create an intermediate image of the sample at the intermediate image plane (IIM). Here, OBJ1 carries an immersion cap (not shown), which establishes a stable contact surface to the water-embedded specimen. Our imaging system thus creates an intermediate image of the object with a lateral magnification $M_{\text{lat}} = 1$ and an axial magnification $M_{\text{ax}} = n_{\text{air}}/n_{\text{water}} = 0.75$.

To excite fluorescence within the specimen, excitation light is generated by a 473 nm laser (MBL-FN-473-100, CNI Laser), which is coupled into a single-mode fiber and collimated by an aspheric lens (F240APC-532, Thorlabs) to create a Gaussian beam with a waist of 10 μm in the specimen. This results in a theoretical confocal parameter, twice the Rayleigh length, of 954 μm. The laser beam is then directed onto a galvanometric scanning mirror (6 mm, 8315 K, Cambridge Technology, SMX), which is placed at the Fourier plane of the second imaging system. Being reflected of a dichroic mirror

(DM), the galvanometric mirror surface is then imaged onto an off-center point at the back focal aperture of the primary imaging objective (OBJ1). This point is chosen to be maximally displaced from the optical axis while preventing occlusion of the excitation beam. For the NA of 0.28 used here, this beam then exits OBJ1 at the corresponding oblique angle of 14.6° (in air, corresponding to 10.9° in water) and can be used to excite fluorescence in an oblique plane by quickly ramping the scanning mirror SMX.

To translate the excited plane through the specimen, we adopt a strategy similar to that used in Refs. [21,25] and use a scanning mirror to scan the excitation light while descanning the emission light.

In our case, the first imaging system contains a large-aperture galvanometric mirror (25 mm beam diameter, 6240H, Cambridge Technology, SMY), which is placed as close as possible to the back focal plane of the objective lens. This imaging geometry leads to an angle of about 14.6° between the emission and the excitation PSF [Fig. 1(b)]. It also leads to the familiar non-rectilinear coordinate system (xyz') of OPM [25], which can be transformed into a conventional coordinate system via an affine transformation consisting of scaling and shearing [Fig. 1(b), Supplement 1].

Because the emission light is descanned, every plane of excited fluorescence is always reimaged onto the same oblique plane at the IIM, which in conventional OPMs is reimaged onto a camera in transmission by a tilted tertiary imaging system. If both systems have the same NA, this inherently leads to the loss of signal, since some of the light propagates outside of the acceptance angle of the tertiary imaging system [Fig. 1(b)]. This problem only gets worse with lower-NA objective lenses and leads to a total loss of all signal at an NA ≤ 0.5. For large-FOV, low-NA objectives such as the 0.28 NA objective used here, the conventional solution to reimaging is therefore inapplicable [Fig. 1(c)].

To enable the reimaging of an oblique plane formed by a low-NA objective lens, we introduced a reflective blazed grating at the intermediate image plane and aligned it to be coplanar with the image of the oblique fluorescence plane [Figs. 1(a) and 1(c)].

Therefore, every point emitter in the excited plane will be imaged and thus focused onto a point on the grating surface. This light focus is then diffracted into multiple orders, emerging at different directions, which can be approximated by the grating equation

$$(m\lambda/d - \sin(\alpha)) = \sin(\beta).$$

In our case, $\lambda = 510$ nm is the central emission wavelength of eGFP, $\alpha = (90 - 14.6)°$ is the incidence angle, β is the diffraction angle with respect to the grating normal, d is the grating period, and m is an integer.

Given these parameters, we chose a commercially available grating with period $d = 555$ nm (GR, Richardson 33025FL01-290R, 26.7° blaze, 1800/mm), which resulted in three allowed diffraction orders $m = -2, -1, 0$ predicted at $\beta = -60.4$, 2.8, and 75.4°, of which the $m = -1$ diffraction order was measured to carry 43% (at $\lambda = 532$ nm) of the incident light. Since the diffracted light in this order propagated almost perpendicularly to the grating, it could now be captured [Fig. 1(d)] by a tertiary imaging system with the identical NA as the reimaging system. The tertiary imaging system consisted of an objective (OBJ3, XLFluor 4×, 0.28 NA) and a tube lens (TL3, TTL 180-A), which imaged the IIM on the grating surface onto a camera (ORCA-Flash4.0 V2, Hamamatsu). We note that although the diffraction grating was a dispersive element, no additional chromatic aberrations were introduced, since the grating surface was imaged directly onto the camera sensor plane (Supplement 1). The camera sensor contained 2048 × 2048 pixels with a pixel pitch of 6.5 μm. We used a region of 2048 × 616 pixels, which corresponded to an effective FOV of 3328 μm (X) × 1001 μm (Z′) at the grating plane. This matched the confocal parameter and approximate axial imaging range of the Gaussian excitation beam. Furthermore, it allowed us to increase the permissible frame rate to 333 Hz. For volumetric imaging, this image plane could be scanned by ±1500 μm in y with help of SMY, resulting in an accessible imaging volume of 3.3 mm × 3.0 mm × 1.0 mm (X × Y × Z).

3. RESULTS

To characterize the optical system, we first imaged a sample of fluorescent beads (diameter 1 μm) dispersed in agarose and recorded images of beads throughout the whole accessible imaging volume [Fig. 2(a)]. Choosing the distance (along y) between the imaging planes to match the effective pixel size of our camera resulted in an isotropic voxel size of 1.625 μm. Example images at increasing distances from the center of the imaging FOV are shown in Fig. 2(b) and exhibit a constant image quality. We then quantified the lateral resolution of our system by calculating the full width at half maximum (FWHM) of the line sections through maximum intensity projections of each bead. The average FWHM values across the FOV were 2.6 ± 1.6 (x) and 3.1 ± 1.8 μm (y). To determine the axial sectioning capability, we

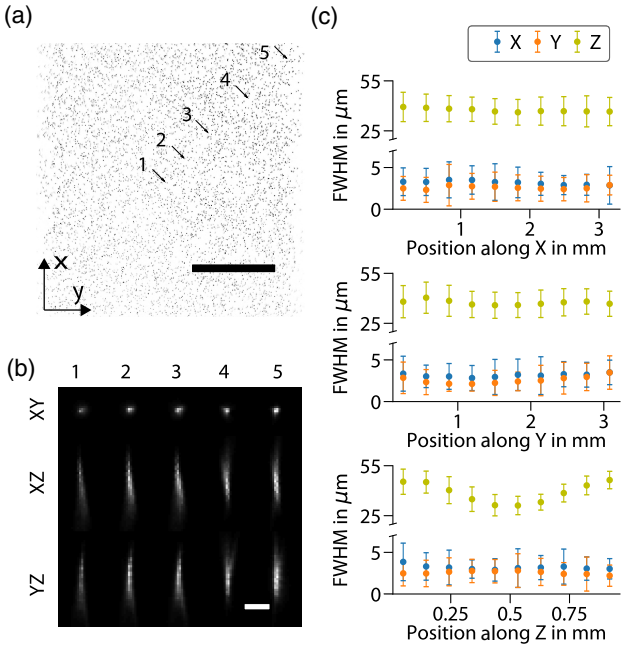

Fig. 2. Quantification of system resolution. (a) Beads in full FOV, maximum intensity projection of bead volume after shear transformation (ST), scale bar 1000 μm. (b) Example beads, maximum intensity projections of five 1 μm sized beads along x, y, and z after ST; the location in the total FOV is indicated by the arrows in (a), scale bar 20 μm. (c) Resolution across the FOV; each plot shows the dependency of the resolution (mean ± SD) along x, y, and z on bead position along x, y, and z (top to bottom).

measured the average FWHM of the axial energy distribution of the microsphere images, calculated as the sum of all pixel values along the *xy* planes of a bead volume and found it to be 37.4 ± 8.4 μm ($n = 3432$). This was constant throughout the FOV, but changed as expected with axial distance from the native image plane due to the broadening of the excitation beam [Fig. 2(c)]. A rough estimate of the information throughput of this imaging configuration can be obtained by dividing its accessible FOV of 3.3 mm × 3.0 mm × 1.0 mm by its volumetric resolution (2.6 × 3.1 × 37.4 μm^3), resulting in 3.5×10^7 resolvable image points. The data throughput of our microscope is limited by the speed of the camera and can be approximated by the amount of resolvable points in one camera frame (3.3 mm × 1.0 mm/(2.6 μm × 37 μm)) multiplied by the maximum frame rate (333 Hz) to yield 11.1 million samples per second (MS/s). To show that we can consistently capture neuronal activity throughout this imaging volume, we recorded the time changing fluorescence of neurons in a restrained zebrafish larva (elavl3:H2B-GCaMP6s, 4 dpf). We translated it to 3 × 3 different extreme points in the FOV [Fig. 3(a)]. At each position, we recorded a time series of the region containing the entire larva (3328 × 382 × 1001 μm^3, 191 planes) at a volume rate of 1.75 Hz and were able to record neural activity. [Fig. 3(b), Supplement 1, Visualization 1]. As a second demonstration, we also imaged the time-dependent fluorescent changes of neurons throughout an entire juvenile zebrafish (elavl3:H2B-GCaMP6s, 33 dpf), an age at which conventional LSM would be challenging due to shadowing effects caused by the eyes and developing skull. We recorded a time series of a 3328 μm × 812 μm × 1001 μm volume, containing the whole fish brain. [s. Fig. 3(b)] Within this volume, we recorded 406 planes at a 2 μm spacing. This enabled us to record from 997 neurons at a volume rate of 0.8 Hz [Figs. 3(d) and 3(e), Supplement 1, Visualization 2].

4. DISCUSSION

The microscope design presented in this paper enables fast volumetric recording of neural activity throughout a volume of 3.3 × 3 × 1.0 mm^3 by capturing imaging data from 333 tilted planes per second. The increase in accessible imaging volume in comparison to previously reported OPM techniques [18–25] is an order of magnitude. We achieve this by using a low-NA objective and modification of the central reimaging step of OPM with the help of a diffraction grating.

While allowing for the use of low-NA objectives with increased FOV, our current implementation has an upper limit for the NA. With two objectives on the same side of a reflective grating, geometrical constraints would limit the maximum possible NA to 0.71 (sin 45°). If desired, this limitation could be overcome by using transmission gratings.

Compared to other OPM techniques, we are trading off photon efficiency and resolution for FOV and flexibility, but there are several ways to improve those quantities (Supplement 1). The efficiency could be further increased by transitioning to a custom-designed 0.5 NA objective lens with a FOV similar to those designed and used in Refs. [2,3]. This would simultaneously increase the resolution, the sectioning capability, and the system bandwidth, allowing it to capture more distinct axial planes. Additionally, the efficiency could be increased by a more efficient

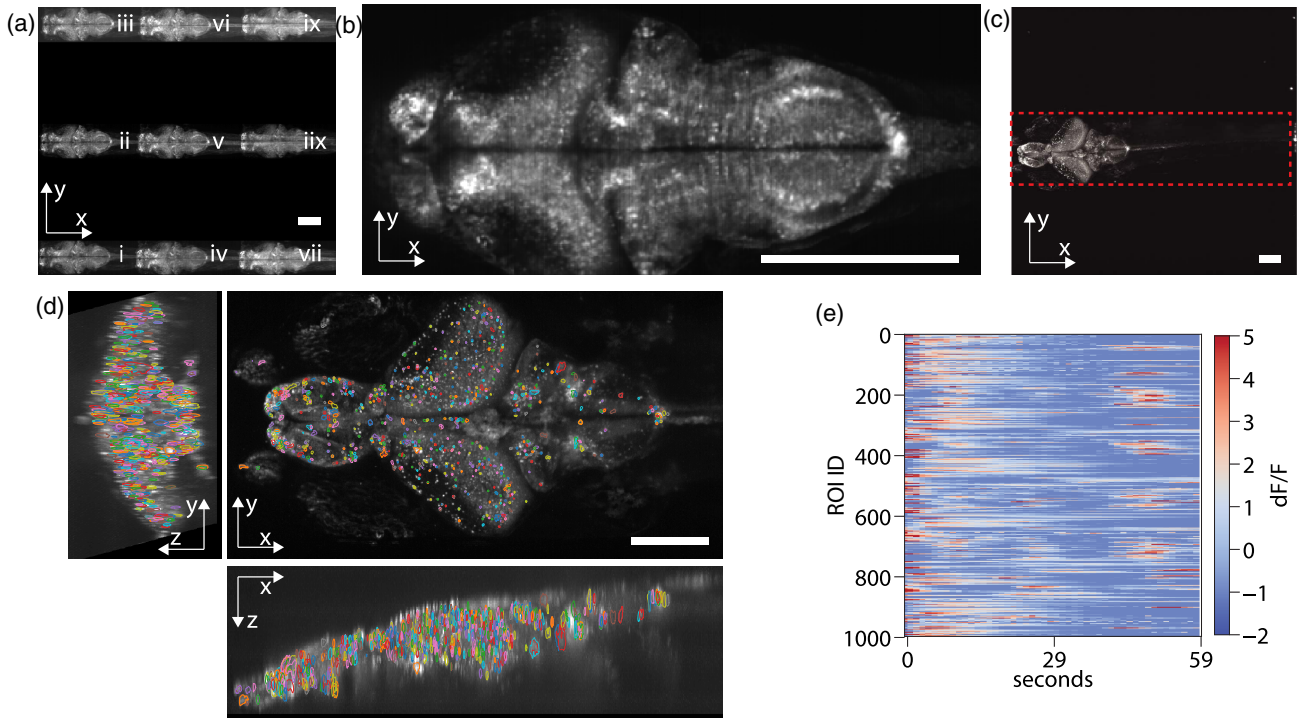

Fig. 3. Measurement of neuronal activity over a large field of view (FOV). (a) Larval zebrafish at different locations across the accessible FOV: montage of a restrained 4dpf Huc:GCaMP6s nuclear zebrafish larva sequentially imaged at nine different locations within the accessible FOV [maximum intensity projection (MIP)]; see Supplement 1, Visualization 1. (b) Slice of the larval zebrafish brain at 100 μm depth and location v. (c) MIP of a 33 dpf Huc:GCaMP6s in the accessible microscope FOV, which was recorded in the time lapse experiments. The dashed red box represents the imaged region. (d) MIP of the brain with overlayed contours of the regions of interest along all three dimensions of the volume; see Supplement 1, Visualization 2. (e) Extracted temporal dF/F traces of the regions of interest shown in (d); scale bar in (a), (b), (c), (d) 250 μm.

diffractive surface. Last, the speed of the technique is currently limited only by the camera speed, but could be increased by implementing a more suitable sampling scheme. Since our microscope captures oblique planes [the *xz* slice in Fig. 2(b)], a Nyquist sampling along the shorter dimension *x* leads to a redundant sampling along *z*. By employing anamorphic optics in the tertiary imaging step, the image could be transformed so that both dimensions are exactly sampled at the Nyquist criterion by the quadratic pixel grid of the camera. This would cut down on the number of acquired pixels per frame and would enable recordings at higher frame rates. This tailored sampling scheme, combined with faster, sensitive cameras, will further increase the sampling rate of this technique.

5. CONCLUSION

Diffractive OPM introduces a new solution for the central reimaging geometry in OPM. It extends the family of these techniques to larger FOVs, and although its resolution is reduced by the use of low-NA objectives, the technique retains OPM's key advantages, such as high speed, a partially parallel detection scheme, true optical sectioning, and a dynamically adjustable region of interest.

Funding. Human Frontier Science Program (HFSP) (RGP0027/2016); H2020 European Research Council (ERC) (ERC-2016-StG-714560); Alfried Krupp von Bohlen und Halbach-Stiftung.

Acknowledgment. We thank Spencer Smith, Thomas Chaigne, Ioannis N. Papadopoulos, Roarke Horstmayer, and Mykola Kadobianskyi for helpful discussions and for critically reading the paper.

See Supplement 1 for supporting content.

REFERENCES

1. W. Denk, J. H. Strickler, and W. W. Webb, "Two-photon laser scanning fluorescence microscopy," Science **248**, 73–76 (1990).
2. J. N. Stirman, I. T. Smith, M. W. Kudenov, and S. L. Smith, "Wide field-of-view, multi-region, two-photon imaging of neuronal activity in the mammalian brain," Nat. Biotechnol. **34**, 857–862 (2016).
3. N. J. Sofroniew, D. Flickinger, J. King, and K. Svoboda, "A large field of view two-photon mesoscope with subcellular resolution for in vivo imaging," eLife **5**, 413 (2016).
4. R. Prevedel, A. J. Verhoef, A. J. Pernía-Andrade, S. Weisenburger, B. S. Huang, T. Nöbauer, A. Fernández, J. E. Delcour, P. Golshani, A. Baltuska, and A. Vaziri, "Fast volumetric calcium imaging across multiple cortical layers using sculpted light," Nat. Methods **13**, 1021–1028 (2016).
5. R. Lu, W. Sun, Y. Liang, A. Kerlin, J. Bierfeld, J. D. Seelig, D. E. Wilson, B. Scholl, B. Mohar, M. Tanimoto, M. Koyama, D. Fitzpatrick, M. B. Orger, and N. Ji, "Video-rate volumetric functional imaging of the brain at synaptic resolution," Nat. Neurosci. **20**, 620–628 (2017).
6. M. Levoy, R. Ng, A. Adams, M. Footer, and M. Horowitz, "Light field microscopy," ACM Trans. Graph. **25**, 924–934 (2006).
7. M. Broxton, L. Grosenick, S. Yang, N. Cohen, A. Andalman, K. Deisseroth, and M. Levoy, "Wave optics theory and 3-D deconvolution for the light field microscope," Opt. Express **21**, 25418–25422 (2013).
8. R. Prevedel, Y.-G. Yoon, M. Hoffmann, N. Pak, G. Wetzstein, S. Kato, T. Schrödel, R. Raskar, M. Zimmer, E. S. Boyden, and A. Vaziri, "Simultaneous whole-animal 3D imaging of neuronal activity using light-field microscopy," Nat. Methods **11**, 727–730 (2014).
9. T. Nöbauer, O. Skocek, A. J. Pernía-Andrade, L. Weilguny, F. M. Traub, M. I. Molodtsov, and A. Vaziri, "Video rate volumetric Ca2+ imaging across cortex using seeded iterative demixing (SID) microscopy," Nat. Methods **14**, 811–818 (2017).
10. L. Cong, Z. Wang, Y. Chai, W. Hang, C. Shang, W. Yang, L. Bai, J. Du, K. Wang, and Q. Wen, "Rapid whole brain imaging of neural activity in freely behaving larval zebrafish (Danio rerio)," eLife **6**, e28158 (2017).
11. S. Abrahamsson, J. Chen, B. Hajj, S. Stallinga, A. Y. Katsov, J. Wisniewski, G. Mizuguchi, P. Soule, F. Mueller, C. D. Darzacq, X. Darzacq, C. Wu, C. I. Bargmann, D. A. Agard, M. Dahan, and M. G. L. Gustafsson, "Fast multicolor 3D imaging using aberration-corrected multifocus microscopy," Nat. Methods **10**, 60–63 (2013).
12. A. Agostinho, A. Jost, D. C. Jans, H. Blom, H. Brismar, K. Bernhem, L. Nilsson, M. Müller, R. Heintzmann, S. Abrahamsson, and T. J. Lambert, "Multifocus structured illumination microscopy for fast volumetric super-resolution imaging," Biomed. Opt. Express **8**, 4135–4140 (2017).
13. B. Hajj, B. Mehl, C. Wu, C. Cho, C. I. Bargmann, J. A. Liddle, J. Wisniewski, J.-B. Fiche, J. Pulupa, L. Oudjedi, L. Chen, L. Yu, M. Davanco, M. Nollmann, M. Dahan, M. El Beheiry, M. Mir, R. Ilic, S. Abrahamsson, T. Lionnet, X. Darzacq, and X. Jin, "Multifocus microscopy with precise color multi-phase diffractive optics applied in functional neuronal imaging," Biomed. Opt. Express **7**, 855–869 (2016).
14. J. Mertz, *Introduction to Optical Microscopy* (Roberts Publishers, 2010).
15. P. J. Keller, A. D. Schmidt, J. Wittbrodt, and E. H. K. Stelzer, "Reconstruction of zebrafish early embryonic development by scanned light sheet microscopy," Science **322**, 1065–1069 (2008).
16. M. B. Ahrens, M. B. Orger, D. N. Robson, J. M. Li, and P. J. Keller, "Whole-brain functional imaging at cellular resolution using light-sheet microscopy," Nat. Methods **10**, 413–420 (2013).
17. J. Huisken, J. Swoger, F. Del Bene, J. Wittbrodt, and E. H. Stelzer, "Optical sectioning deep inside live embryos by selective plane illumination microscopy," Science **305**, 1007–1009 (2004).
18. C. Dunsby, "Optically sectioned imaging by oblique plane microscopy," Opt. Express **16**, 20306–20316 (2008).
19. A. R. Lyon, C. Dunsby, D. Wilding, K. T. MacLeod, M. B. Sikkel, and S. Kumar, "Application of oblique plane microscopy to high speed live cell imaging," Proc. SPIE **8086**, 80860V (2011).
20. S. Kumar, D. Wilding, M. B. Sikkel, A. R. Lyon, K. T. MacLeod, and C. Dunsby, "High-speed 2D and 3D fluorescence microscopy of cardiac myocytes," Opt. Express **19**, 13839–13847 (2011).
21. M. B. Bouchard, V. Voleti, C. S. S. Mendes, C. Lacefield, W. B. Grueber, R. S. Mann, R. M. Bruno, and E. M. C. Hillman, "Swept confocally-aligned planar excitation (SCAPE) microscopy for high-speed volumetric imaging of behaving organisms," Nat. Photonics **9**, 113–119 (2015).
22. M. B. Sikkel, S. Kumar, V. Maioli, C. Rowlands, F. Gordon, S. E. Harding, A. R. Lyon, K. T. MacLeod, and C. Dunsby, "High speed sCMOS-based oblique plane microscopy applied to the study of calcium dynamics in cardiac myocytes," J. Biophoton. **9**, 311–323 (2016).
23. B. Huang, D. Xie, and R. Mcgorty, "High-NA open-top selective-plane illumination microscopy for biological imaging," Opt. Express **25**, 17798–17810 (2017).
24. Y. Shin, D. Kim, and H.-S. Kwon, "Oblique scanning 2-photon light-sheet fluorescence microscopy for rapid volumetric imaging," J. Biophoton. **11**, e201700270 (2018).
25. M. Kumar, S. Kishore, J. Nasenbeny, D. L. McLean, and Y. Kozorovitskiy, "Integrated one-and two-photon scanned oblique plane illumination (sopi) microscopy for rapid volumetric imaging," Opt. Express **26**, 13027–13041 (2018).
26. M. Kumar and Y. Kozorovitskiy, "Tilt-invariant scanned oblique plane illumination microscopy for large-scale volumetric imaging," Opt. Lett. **44**, 1706–1709 (2019).
27. R. D. Vaadia, W. Li, V. Voleti, A. Singhania, E. M. C. Hillman, and W. B. Grueber, "Characterization of proprioceptive system dynamics in behaving Drosophila larvae using high-speed volumetric microscopy," Curr. Biol. **29**, 935–944 (2019).
28. E. J. Botcherby, R. Juškaitis, M. J. Booth, and T. Wilson, "An optical technique for remote focusing in microscopy," Opt. Commun. **281**, 880–887 (2008).
29. A. W. Lohmann, "Scaling laws for lens systems," Appl. Opt. **28**, 4996–4998 (1989).
30. S. J. Drake, "Systems and methods for forming an image of a specimen at an oblique viewing angle," PCT Patent WO2003027644A1 (April3, 2003).